12th International Symposium on Turbulence and Shear Flow Phenomena (TSFP12)
Osaka, Japan, July 19–22, 2022

HIGH-REYNOLDS NUMBER EFFECTS IN SHOCK-WAVE/TURBULENT BOUNDARY-LAYER INTERACTIONS

L. Laguarda*, S. Hickel, F. F. J. Schrijer and B. W. van Oudheusden

Aerodynamics Group, Faculty of Aerospace Engineering
Delft University of Technology
Kluyverweg 1, 2629HS Delft, The Netherlands
*L.LaguardaSanchez@tudelft.nl

ABSTRACT

We investigate Reynolds number effects in shock-wave/turbulent boundary-layer interactions (STBLI) with strong mean flow separation. Three wall-resolved large-eddy simulations (LES) are performed for this purpose, with different Reynolds number but otherwise equal flow parameters and simulation setup. The resulting LES data covers more than a decade of friction Reynolds number. The high-Reynolds case, with friction Reynolds number $Re_\tau = 5118$ and momentum Reynolds number $Re_\theta = 26438$ at the virtual impingement point without the shock, features a turbulent boundary layer with clear inner and outer scale separation. All STBLI simulations exhibit substantial flow reversal and have been integrated for a very long time (90 flow-through times of the full domain length) to properly resolve low-frequency dynamics. Instantaneous and mean flow as well as spectral features are described in detail, together with a modal analysis of the three-dimensional streamwise velocity, streamwise vorticity and pressure fields.

1 INTRODUCTION

Interactions between shock waves and turbulent boundary layers (STBLI) occur in many high-speed applications such as supersonic air intakes and rocket nozzles. For strong interaction, where substantial separation occurs, STBLI have been found to be highly dynamic and complex and have critical effects on aerodynamic efficiency, noise generation and system lifetime (Délery & Dussauge, 2009).

Despite the considerable attention that STBLI have received in the past decades, there are fundamental aspects that remain unclear. One of such aspects is the effect of Reynolds number on the interaction dynamics. Due to the high computational costs associated with the numerical simulation of STBLI, previous numerical works were limited to moderate Reynolds numbers, often lower than complementary experimental investigations. A systematic analysis of Reynolds number effects is therefore needed for a more comprehensive understanding of the practically relevant high-Reynolds regime of STBLI.

2 CASE STUDY AND NUMERICAL SETUP

We consider an oblique shock impinging on a flat-plate turbulent boundary layer (TBL). Flow parameters are selected such as to ensure exact experimental reproducibility of the high-Reynolds case in TU Delft wind tunnels. All simulations have a free-stream Mach number of $M = 2.0$ and stagnation temperature and pressure of $T_0 = 288$ K and $p_0 = 356$ kPa. The 99% velocity-based boundary layer thickness at the inflow plane $\delta_{99,i}$ is 5.2 mm. The incident shock angle is set to $\phi = 40.04^\circ$ and corresponds to a flow deflection of $\vartheta = 10.66^\circ$. The wall is modeled as isothermal at the free-stream stagnation temperature, i.e., $T_{wall} = T_0$.

The computational domain is rectangular with dimensions $[L_x, L_y, L_z] = [45, 16.5, 4]\delta_{99,i}$. Non-reflecting boundary conditions are used at the top and outflow boundaries, and periodicity is imposed in the spanwise direction. The incident shock is introduced by prescribing Rankine-Hugoniot relations at the top boundary, and the virtual impingement point on the wall, referred to as x_{imp}, is located $32\delta_{99,i}$ downstream of the inflow plane. The digital filter technique of Xie & Castro (2008) is used to prescribe adequate turbulent boundary conditions with well-defined space and time correlations at the inflow.

Simulations are performed with INCA (https://www.inca-cfd.com), an in-house solver that employs a finite volume method and a third-order Runge-Kutta scheme for the discretization of the compressible Navier-Stokes equations. The numerical method ensures consistency of shock-capturing and sub-grid scale turbulence modelling using the adaptive local deconvolution method (ALDM), see Hickel *et al.* (2014) for implementation and verification details.

3 RESULTS

Undisturbed TBL characteristics

Characterizing the undisturbed TBL is particularly instructive for the present analysis since Reynolds effects in STBLI stem from the fundamental differences of the TBL structure at low and high Reynolds number. For this purpose, additional simulations were conducted without the incident shock and relevant quantities were measured at x_{imp}. Table 1 provides a summary of relevant boundary layer parameters at this location together with the color legend used throughout the paper. The present study covers more than a decade of friction Reynolds number Re_τ, with the largest value being $Re_\tau = 5116$ for case B3. This value is a factor three larger than previous high-fidelity numerical investigations of canonical STBLI (Pasquariello *et al.*, 2017).

The corresponding density-scaled Reynolds stresses at x_{imp} are presented in Figure 1 and exemplary illustrate Reynolds number effects in the TBL topology. Most notably,

Table 1. Relevant parameters of the undisturbed TBL. Re_τ is defined with wall quantities and δ_{99}, while Re_θ is based on free-stream values and the momentum thickness θ (compressible form).

Case	$\delta_{99}/\delta_{99,i}$	Re_τ	Re_θ	Legend
B1	1.47	355	1577	Gray
B2	1.37	1226	5733	Blue
B3	1.39	5118	26438	Black

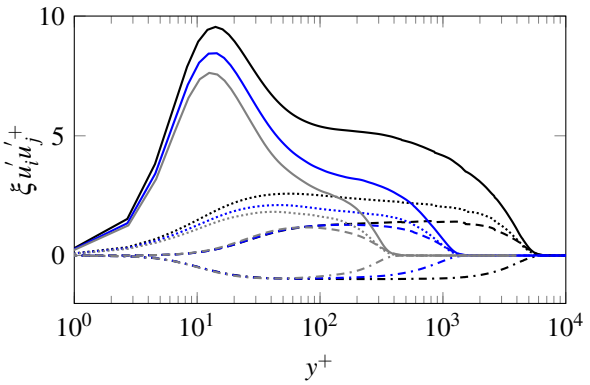

Figure 1. Density-scaled Reynolds stresses at the inviscid impingement location in the absence of the shock: streamwise (solid), wall-normal (dashed), spanwise (dotted) and shear (dash-dotted). See Table 1 for color legend.

there is a clear increase in fluctuation intensity for the wall-parallel components with Re_τ. This is a consequence of the emergent large-scale coherent motions in the near-logarithmic region, which for case B3 extends more than a decade of inner-scaled wall distance (indicated by the plateau in the shear stress distribution). The observed increase in streamwise stress near the wall also reveals the modulating influence that such outer-layer motions have on the near-wall cycle (Hutchins & Marusic, 2007). Peak values in Figure 1 for this stress are in very good agreement with the reference DNS data of Pirozzoli & Bernardini (2011, 2013) for supersonic TBLs at similar conditions.

Inspection of streamwise spectra (not shown here) reveals a clear bimodal distribution for case B3, exhibiting an inner peak at a wavelength $\lambda_x^+ \approx 700$ and an outer peak at $\lambda_x \approx 6\delta_{99}$. While evidencing scale separation and the genuinely high-Reynolds nature of this case, the largest scales are still not expected to meaningfully alter the low-frequency dynamics of STBLI (Clemens & Narayanaswamy, 2014). Spanwise spectra of streamwise velocity fluctuations are shown in Figure 2 for all cases. As observed, spectra at $y^+ \approx 15$ excellently collapse at high wavenumbers when inner scaling is employed, see Figure 2(a). At low wavenumber, however, a distinct peak appears for case B3 due to the imprint of outer-layer motions on the near-wall cycle. Spectra in outer scaling at $y/\delta_{99} \approx 0.1$, shown in Figure 2($b$), show a reasonable agreement at low wavenumbers. Wavelengths associated with peak values provide an indication of the spanwise spacing of large-scale motions, which for case B3 is approximately $\lambda_z \approx 0.8\delta_{99}$. We also note that cases B2 and B3 collapse well in Figure 2(b) along the inertial sub-range, which extends for over a decade

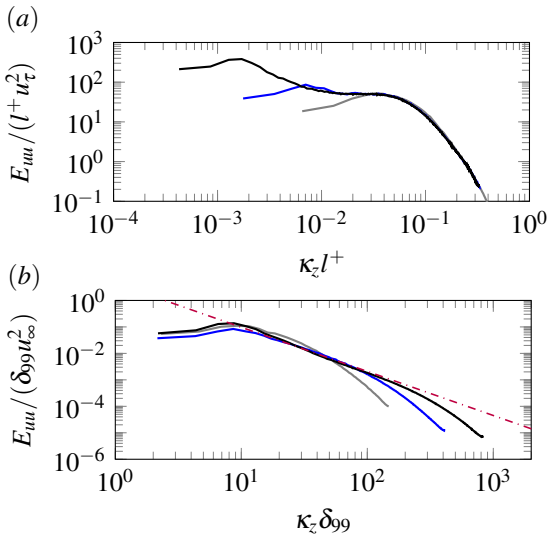

Figure 2. Spanwise spectra of streamwise velocity fluctuations at (a) $y^+ \approx 15$ in inner scaling, and (b) $y/\delta_{99} \approx 0.1$ in outer scaling. Dash-dotted line denotes $\kappa_z^{-5/3}$ behavior.

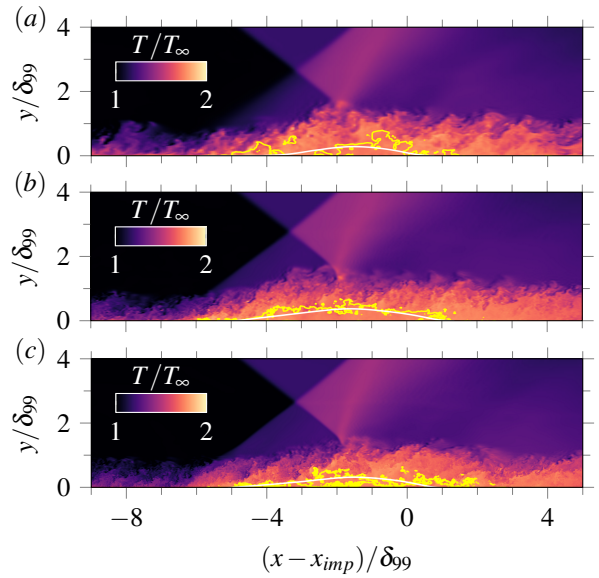

Figure 3. Instantaneous temperature fields: (a) case B1, (b) case B2, and (c) case B3. Solid lines indicate instantaneous (yellow) and mean (white) isocontours of zero streamwise velocity.

with close $\kappa_z^{-5/3}$ behavior.

Instantaneous and mean STBLI organization

Instantaneous impressions of the temperature field are provided in Figure 3 and illustrate the investigated STBLI topology. The adverse pressure gradient imposed by the incident shock is strong enough to cause substantial flow separation in all cases. Solid lines indicate instantaneous (yellow) and mean (white) contours of zero streamwise velocity. For cases B2 and B3, the separation shock is a sharp discontinuity that emanates from deep within the TBL; for case B1, on the other hand, the compression fan generated at the leading edge of the separated flow region is only coalescing into a shock wave well outside the TBL. This is directly linked to the

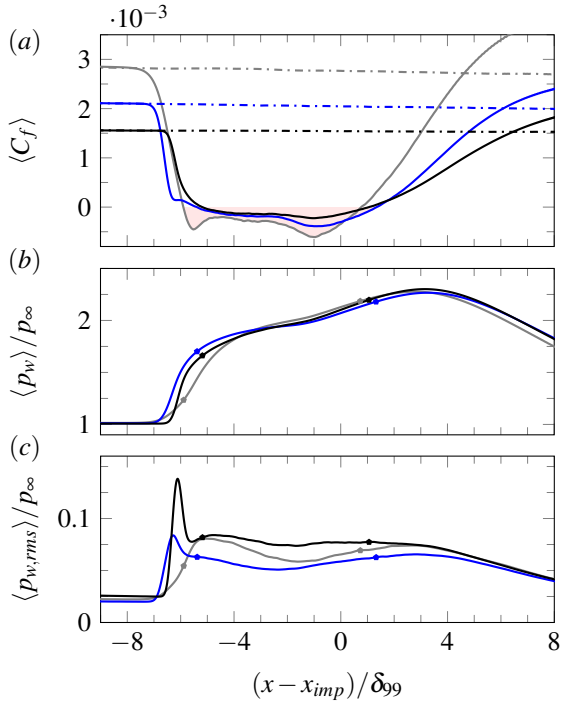

Figure 4. Time- and spanwise-averaged (a) skin friction, (b) wall-pressure, and (c) wall-pressure fluctuation intensity. Separated regions in (a) are shaded in red and dash-dotted lines denote the corresponding skin friction distribution for the undisturbed TBLs. Mean separation and reattachment points in (b) and (c) are indicated with a marker.

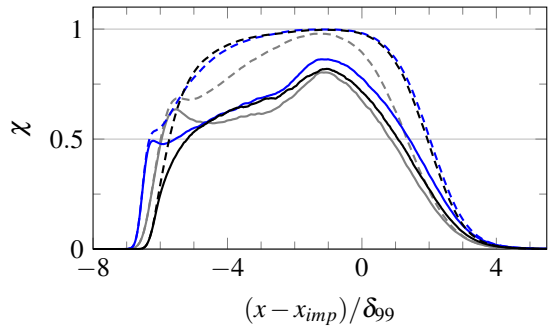

Figure 5. Spanwise-averaged probability of reverse flow: at the wall (solid lines) and maximum value (dashed lines).

height of the sonic line (from which compression waves emanate), which is Reynolds number dependent and dictates the intensity of the separation shock footprint on the surface.

At the separation shock foot, the flow is strongly decelerated and starts to detach. Disturbances from the upstream TBL are seeded into the detaching shear layer. As the shear layer core moves further away from the wall, large vortical structures are formed, which eventually interact with the incident-transmitted shock tip at the bubble apex. Such shock-vortex interaction and the strong flow deceleration at separation correspond to visible peaks in the turbulence kinetic energy production. Immediately after the bubble apex, however, turbulence is damped. The strong convex streamline curvature results in an expansion fan that turns the flow towards the wall and initiates the reattachment process. All STBLI cases exhibit a very mild concave streamline curvature at reattachment, which results in a weak compression fan instead of a coalesced reattachment shock.

Relevant wall-properties are presented in Figure 4. Skin friction distributions, shown in Figure $4(a)$, reveal the extent of the separated regions as well as the upstream influence on the incoming TBLs. All C_f profiles reach their maximum negative values slightly upstream of the reattachment point. The separation length L_{sep}, defined as the distance between mean separation and reattachment points, is $L_{sep} = 6.68\delta_{99}$ for case B1, $L_{sep} = 6.74\delta_{99}$ for case B2, and $L_{sep} = 6.25\delta_{99}$ for case B3. Beyond reattachment, skin friction overshoots the corresponding levels for the undisturbed TBLs (dash-dotted lines) due to the expansion fan that originates at the trailing edge of the (virtual) shock generator.

Figures $4(b)$ and $4(c)$ show the wall-pressure and wall-pressure RMS distributions, and they clearly illustrate the effect of Reynolds number on STBLI. While cases B2 and B3 display an abrupt rise in surface pressure, case B1 shows a much smoother increase. This indicates the presence of a compression fan at separation instead of a coalesced shock, as anticipated in Figure $3(a)$ for the low-Reynolds case. Such compression fan does not leave a visible footprint on the wall pressure RMS, whereas the other cases (B2 and B3) clearly exhibit a peak in pressure fluctuation before separation. This peak is attributed to the separation shock dynamics and increases in magnitude with Reynolds number. Figure $4(b)$ also reveals an incipient pressure plateau for cases B2 and B3, although it is not fully established in either case because of the moderate incident shock strength. Right after separation, pressure RMS levels remain high (reaching the global maximum for case B1 and a local maximum for case B3) due to the flapping motion of the shear layer. This is followed by a small drop in pressure fluctuation intensity within the separated region before increasing again as a result of the reattaching shear layer vortices. We note that mean separation beyond the pressure fluctuation intensity peak in Figure $4(c)$ is also a consequence of the moderate incident shock strength. For cases B2 and B3, a deeper penetration into the interaction region is on average required for the high-momentum flow to detach from the wall.

Moreover, the probability of reversed flow χ is shown in Figure 5 for all cases. Solid lines indicate flow reversal at the wall, while dashed lines consider the maximum value, i.e., flow reversal at any point in the wall-normal direction. For the lower Reynolds cases, an initial peak appears at separation indicating the presence of an incipient recirculation region with partial reattachment (e.g., see the local maximum at $(x - x_{imp})/\delta_{99} \approx -5.6$ for case B1, which is also present in Figure $4(a)$ for the skin friction distribution). This is not observed for the high-Reynolds case B3, where the separated flow is rapidly lifted away from the wall. All cases exhibit a maximum in reverse flow probability slightly before x_{imp}, being almost unity for cases B2 and B3 when all wall-normal locations are considered.

In order to illustrate the effect of incoming TBL outer-layer structures on the STBLI organization, we show in Figure $6(a)$ the instantaneous three-dimensional flow configuration for case B3 in terms of streamwise velocity fluctuation. From the rendering, it is clear that incoming regions of low- and high-momentum fluid, which appear spaced more than $0.5\delta_{99}$ apart in span (in agreement with the spectra of Figure $2(b)$), affect also the detached shear layer topology. As a result of their passage through the interaction, these regions re-organize into structures with clearly larger spatial coherence beyond reattachment. At separation, the passage of low- and high-momentum fluid results in a strong spanwise modulation of the separation shock (Wu & Martin, 2008; Humble

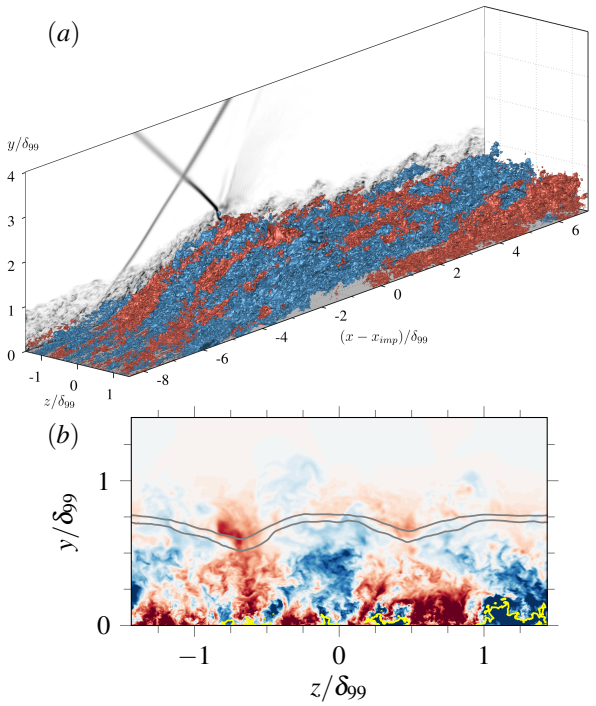

Figure 6. Instantaneous flow configuration for case B3: (a) three-dimensional isocontours of streamwise velocity fluctuation (blue/red: $u'/u_\infty = \pm 0.12$), and (b) corresponding two-dimensional visualization at $(x-x_{imp})/\delta_{99} = -5.62$ (from blue to red: $u'/u_\infty = -0.2$ to $u'/u_\infty = 0.2$). Solid lines in (b): separation shock location (gray, $|\nabla p|\delta_{99}/p_\infty = 4$) and separated flow region (yellow, $u = 0$).

et al., 2009). Such effect can be clearly seen in Figure 6(b), the corresponding streamwise-normal slice of Figure 6(a) at $(x-x_{imp})/\delta_{99} = -5.62$. As observed, the proximity of the separation shock to the wall and the absence of separated flow are clearly correlated with the passage of high-speed fluid.

Spectral analysis

In order to identify dominant frequencies in the investigated STBLIs, we analyze temporal spectra of wall pressure, separation shock location and deflection, and bubble volume. Power spectral densities (PSD) have been estimated using Welch's algorithm, with Hamming windows and 10 segments with 65% overlap (segment length of approximately $100L_{sep}/u_\infty$).

The wall pressure PSD at the domain centerline is shown in Figures 7(a)-7(c) for all cases. They illustrate one of the most prominent features of STBLI, that is, to shift the broadband high-frequency content in the upstream TBL to much lower frequencies. In agreement with previous works (e.g., Pasquariello *et al.* (2017)), the separation shock exhibits broadband low-frequency dynamics that extend from a Strouhal number $S_{t_{L_{sep}}} = fL_{sep}/u_\infty$ of approximately 0.1 to 0.01 and lower. The spatial extent associated with such dynamics (representative of the streamwise excursion of the separation shock) is of the order of one boundary layer thickness. For the low-Reynolds case B1 in Figure 7(a), the separation shock low-frequency dynamics do not appear as energetic as in the other cases. Wall pressure signals in this region exhibit a probability density function that is almost Gaussian for this case, while it is bimodal and highly skewed for case B2 and most notably for the high-Reynolds case B3. This is characteristic of strongly intermittent signals. Furthermore, vertical red lines in Figures 7(b) and 7(c) indicate mean separation and reattachment locations. It is clear that separation occurs downstream of the separation shock excursion range for cases B2 and B3. The reattachment region, on the other hand, is associated with more than two continuous decades of energetic frequencies for all cases. These include: $S_{t_{L_{sep}}}$ larger than unity, characteristic of small scale turbulence; intermediate frequencies around $S_{t_{L_{sep}}} \approx 0.5$, related to the reattaching shear layer vortices (Dupont *et al.*, 2006); and $S_{t_{L_{sep}}} \lesssim 0.1$, corresponding to low-frequency motions of the reattachment line. The latter are also found in the rear part of the separation bubble, at the streamwise location where the skin friction distributions in Figure 4(a) exhibit a global minima ($(x-x_{imp})/\delta_{99} \approx -1$), and they appear more energetic with Reynolds number.

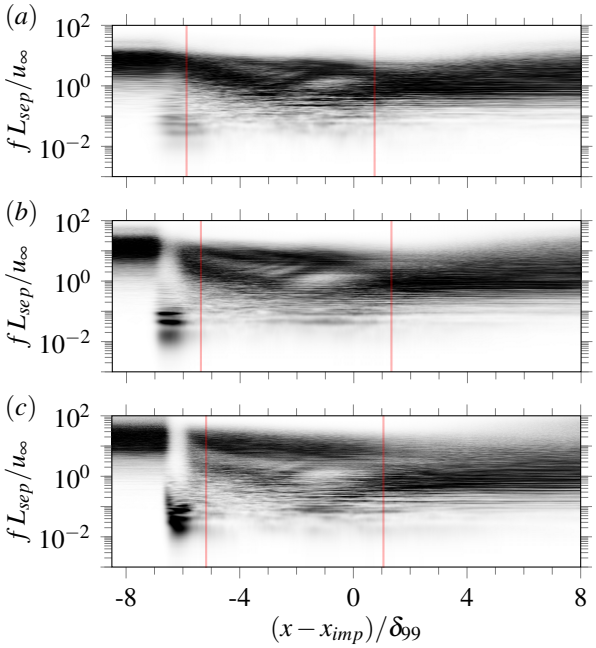

Figure 7. Frequency weighted PSD map of surface pressure at the center line: (a) case B1, (b) case B2, and (c) case B3. Red lines indicate mean separation and reattachment locations.

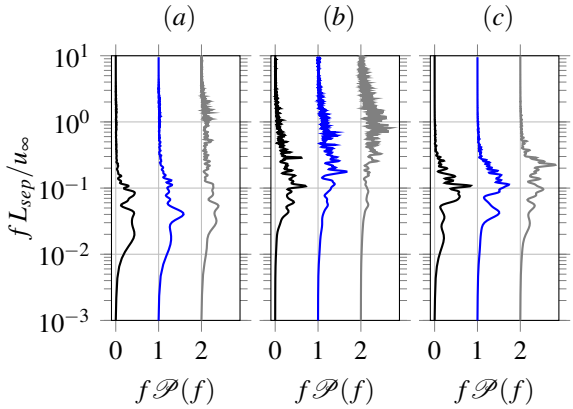

Figure 8. Frequency weighted PSD of (a) spanwise-averaged separation shock location (b) spanwise-averaged separation shock deflection, and (c) separation bubble volume. Data for B1 and B2 are offset for clarity.

Figures 8(a)-8(c) show the PSDs associated with the separation shock location, separation shock deflection and bubble

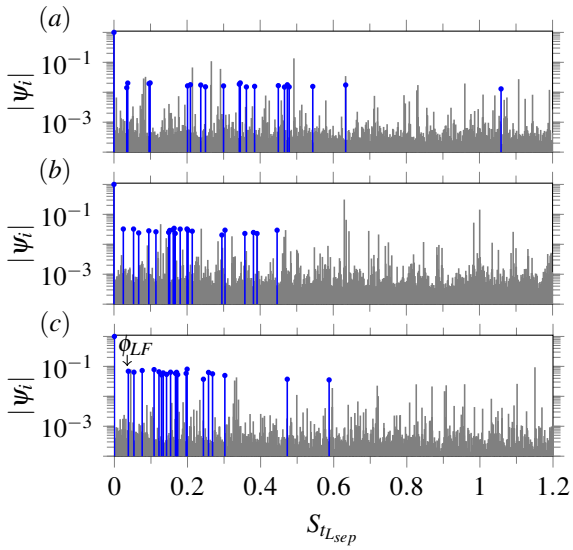

Figure 9. Normalized DMD amplitudes: (a) case B1, (b) case B2, and (c) case B3. Standard DMD solution (Schmid, 2010) is indicated in gray, while dynamically relevant modes identified with SPDMD (Jovanović *et al.*, 2014) appear as blue bars with a marker.

volume. While the low-frequency tone of the separation shock motion is apparent, see Figure 8(a), intermediate frequencies have a stronger contribution to the separation shock deflection, see Figure 8(b). The spectrum for the bubble volume in Figure 8(c) also exhibits energetic low-frequency content related to the separation shock excursion. Interestingly, the spectra clearly peaks at $S_{t_{L_{sep}}} \approx 0.1$ for the higher Reynolds number cases. Is not yet clear what causes such a distinct peak, but we note that the spectra for the separation shock deflection also exhibits energetic content around $S_{t_{L_{sep}}} \approx 0.1$ (particularly for case B3). This suggests a statistical link between the two at this frequency. In line with the work of Wu & Martin (2008), we also find a peak in the cross-correlation between bubble volume and separation shock location signals for a small negative lag. This agrees with the notion that separation shock excursions are preceded by bubble volume variations, specially considering that the time lag we observe is approximately the time required by a pressure disturbance generated at reattachment to reach the separation shock foot.

Modal analysis

In order to relate global flow phenomena to the energetic frequencies identified in the spectral analysis, we additionally perform dynamic mode decomposition (DMD, Schmid (2010)) of the LES data. For impinging STBLI, such modal analysis technique is usually applied to two-dimensional datasets, often resulting from spanwise averaging (e.g. Pasquariello *et al.* (2017); Nichols *et al.* (2017)). Here, we instead perform DMD of a full three-dimensional data set that includes instantaneous streamwise velocity, pressure and streamwise vorticity. In total, 8192 snapshots recorded at a sampling interval of $0.5\delta_{99,i}/u_\infty$ are used for each case. In addition, further dimensionality reduction is sought by employing the sparsity-promoting DMD algorithm (SPDMD, Jovanović *et al.* (2014)) in order to identify the 41 most dynamically relevant modes from the standard DMD solution.

Figures 9(a)-(c) show normalized SPDMD modal amplitudes for each case together with the corresponding standard DMD amplitudes within the same frequency range. Since

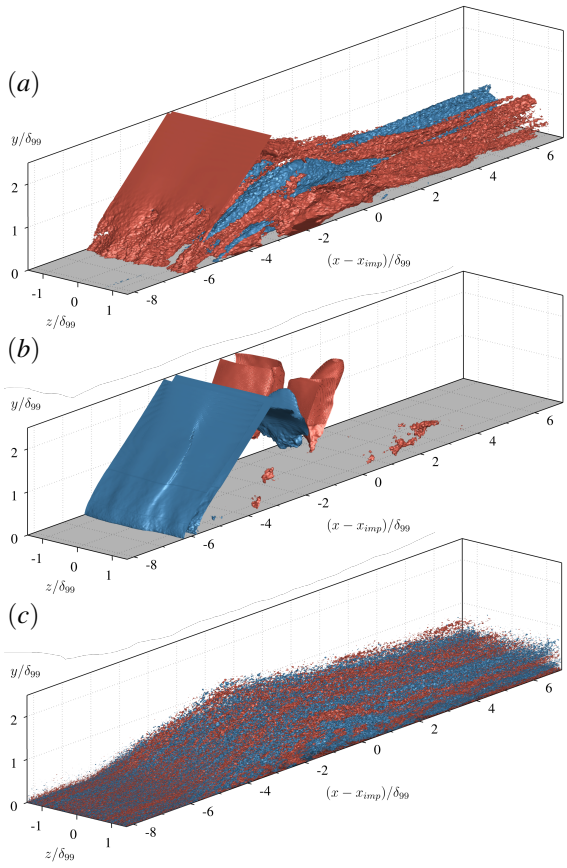

Figure 10. Isosurfaces of mode ϕ_{LF} in Figure 9(c) with phase angle $\theta = \pi/4$: (a) streamwise velocity, (b) pressure, and (c) streamwise vorticity (red/blue indicate positive/negative fluctuation).

snapshot data is real valued and modes with non-zero frequencies arise as complex conjugate pairs, we omit the negative part of the frequency spectrum. As observed, all SPDMD solutions have a similar structure: a mean mode and 20 complex conjugate pairs concentrated on the intermediate frequency range ($S_{t_{L_{sep}}} \approx 0.1$ to 0.6) and low frequency range ($S_{t_{L_{sep}}} \lesssim 0.1$). With the exception of one mode for case B1, the SPDMD algorithm has removed dynamic modes with frequencies above $S_{t_{L_{sep}}} = 1$ from the sparse approximation in all cases. Such concentration towards lower frequencies is in very good agreement with the spectral analysis discussed above. We also note that, in line with the three-dimensional DMD of a Mach 2.9 compression ramp flow by Priebe *et al.* (2016), the contribution of all SPDMD modes in the broadband intermediate and low frequency ranges are required to reconstruct the corresponding STBLI dynamics.

Mode ϕ_{LF} from Figure 9(c) is selected as representative for the low-frequency SPDMD modes below $S_{t_{L_{sep}}} = 0.1$ (modes in this frequency range are qualitatively similar for the other cases). Isosurfaces of velocity, pressure and streamwise vorticity for this mode are included in Figures 10(a)-10(c). While the large-amplitude separation shock excursion is quite coherent in span, see Figures 10(a) and 10(b), other three-dimensional features are evident. For instance, alternating regions of low- and high-speed fluid that re-organize near reattachment, see Figure 10(a). These structures bear qualitative resemblance to those in Figure 6. Additionally, modal streamwise vorticity flucutations in Figure 10(c) clearly reveal large-scale counter-rotating streamwise vortices, forming at and ex-

tending beyond reattachment. These structures, often referred to as Görtler-like vortices (Priebe *et al.*, 2016; Pasquariello *et al.*, 2017), appear spaced approximately one boundary layer thickness in span and meander for different phases of the presented mode. Although statistically linked, we note that this correlation is not sufficient to conclude that such vortices are the cause of shock motion.

Inspection of modal pressure at different frequencies reveals a frequency-dependent asynchronous motion between the separation shock and the incident-transmitted shock. A phase shift of approximately $\pi/2$ is observed for modal frequencies below $S_{t_{L_{sep}}} \approx 0.1$. For higher modal frequencies, this phase shift increases to approximately π in all cases. Regarding the separation shock motion, its excursion range becomes narrower with increasing modal frequency and its spanwise coherence also decreases. This implies larger shock deflection variations and a stronger spanwise modulation at such frequencies, which accentuate for the high-Reynolds case B3.

Lastly, we note that all SPDMD solutions include a mode at $S_{t_{L_{sep}}} \approx 0.1$, which has been identified as dominant in the spectral analysis (see Figures $8(b)$ and $8(c)$). Its modal shape (not shown here) bears similarities with those modes in the low-frequency range (such as ϕ_{LF}, shown in Figure 10). However, the excursion range of the separation shock is slightly shorter, in line with higher frequency modes, and the separation shock motion at the domain centerline appears slightly delayed with that at the side boundaries. At the same time, disturbances are seen to propagate along the shock direction.

4 CONCLUSIONS

We have discussed Reynolds number effects in impinging STBLI with strong mean flow separation. Instantaneous and mean flow configurations illustrate the increasing separation shock footprint at the wall and spanwise modulation of the separation shock at high Reynolds number. Spectral analysis of wall-pressure and separation-shock location confirms the broadband low-frequency dynamics of the separation shock. In turn, spectral densities of shock deflection and separation bubble volume have a distinct peak at the separation-length-based Strouhal number $S_{t_{L_{sep}}} \approx 0.1$, which appears more prominent at high Reynolds number. We are currently investigating the potential mechanisms driving such frequency. In line with the work of Wu & Martin (2008), we also find that the separation shock motion lags that of the separation bubble in all cases. We find that the time lag between both signals is approximately equal to the time required by a pressure disturbance generated at reattachment to reach the separation-shock foot. Sparsity promoting dynamic mode decomposition (SPDMD) of three-dimensional streamwise velocity, pressure and streamwise vorticity fields identified the dynamically most important modes, which clearly concentrate at low to moderate frequencies. Inspection of modal shapes reveal streamwise velocity fluctuation coherence across the interaction at low frequencies as well as a frequency-dependent phase offset between the separation and incident-transmitted shocks (ranging from $\pi/2$ to π). Additionally, our modal analysis unambiguously confirms the presence of Görtler-like vortices statistically linked to the large-amplitude separation shock excursion in all cases. However, the observed correlation is not sufficient to conclude that such vortices are the cause of shock motion.

ACKNOWLEDGMENETS

We acknowledge PRACE for awarding us access to HAWK, a supercomputer of the High Performance Computing Center (HLRS) in Stuttgart, Germany.

REFERENCES

Clemens, Noel T & Narayanaswamy, Venkateswaran 2014 Low-frequency unsteadiness of shock wave/turbulent boundary layer interactions. *Annual Review of Fluid Mechanics* **46**, 469–492.

Délery, Jean & Dussauge, Jean-Paul 2009 Some physical aspects of shock wave/boundary layer interactions. *Shock Waves* **19** (6), 453.

Dupont, P, Haddad, C & Debieve, JF 2006 Space and time organization in a shock-induced separated boundary layer. *Journal of fluid Mechanics* **559**, 255–277.

Hickel, Stefan, Egerer, Christian P & Larsson, Johan 2014 Subgrid-scale modeling for implicit large eddy simulation of compressible flows and shock-turbulence interaction. *Physics of Fluids* **26** (10), 106101.

Humble, RA, Elsinga, GE, Scarano, F & Van Oudheusden, BW 2009 Three-dimensional instantaneous structure of a shock wave/turbulent boundary layer interaction. *Journal of Fluid Mechanics* **622**, 33–62.

Hutchins, Nicholas & Marusic, Ivan 2007 Large-scale influences in near-wall turbulence. *Philosophical Transactions of the Royal Society A: Mathematical, Physical and Engineering Sciences* **365** (1852), 647–664.

Jovanović, Mihailo R, Schmid, Peter J & Nichols, Joseph W 2014 Sparsity-promoting dynamic mode decomposition. *Physics of Fluids* **26** (2), 024103.

Nichols, Joseph W, Larsson, Johan, Bernardini, Matteo & Pirozzoli, Sergio 2017 Stability and modal analysis of shock/boundary layer interactions. *Theoretical and Computational Fluid Dynamics* **31** (1), 33–50.

Pasquariello, Vito, Hickel, Stefan & Adams, Nikolaus A 2017 Unsteady effects of strong shock-wave/boundary-layer interaction at high reynolds number. *Journal of Fluid Mechanics* **823**, 617–657.

Pirozzoli, Sergio & Bernardini, Matteo 2011 Turbulence in supersonic boundary layers at moderate reynolds number. *Journal of Fluid Mechanics* **688**, 120–168.

Pirozzoli, Sergio & Bernardini, Matteo 2013 Probing high-reynolds-number effects in numerical boundary layers. *Physics of Fluids* **25** (2), 021704.

Priebe, Stephan, Tu, Jonathan H, Rowley, Clarence W & Martín, M Pino 2016 Low-frequency dynamics in a shock-induced separated flow. *Journal of Fluid Mechanics* **807**, 441–477.

Schmid, Peter J 2010 Dynamic mode decomposition of numerical and experimental data. *Journal of fluid mechanics* **656**, 5–28.

Wu, Minwei & Martin, M Pino 2008 Analysis of shock motion in shockwave and turbulent boundary layer interaction using direct numerical simulation data. *Journal of Fluid Mechanics* **594**, 71–83.

Xie, Zheng-Tong & Castro, Ian P 2008 Efficient generation of inflow conditions for large eddy simulation of street-scale flows. *Flow, Turbulence and Combustion* **81** (3), 449–470.